Thermal Drude weight in an integrable chiral clock model

Sandipan Manna and G. J. Sreejith
IISER Pune, Dr Homi Bhabha Rd, Pune 411008, India

(Received 19 May 2023; revised 26 July 2023; accepted 27 July 2023; published 10 August 2023)

We calculate the finite temperature thermal conductivity of a time-reversal invariant chiral $\mathbb{Z}_3$ clock model along an integrable line in the parameter space using the time-dependent density matrix renormalization group. The thermal current itself is not a conserved charge, unlike in the case of XXZ model, but has a finite overlap with a local conserved charge $Q^{(2)}$ obtained from the transfer matrix. We find that the Drude weight is finite at nonzero temperature, and the Mazur bound from $Q^{(2)}$ saturates the Drude weight, allowing us to obtain an asymptotic expression for the Drude weight at high temperatures. The numerical estimates of the conductivity are validated using a sum rule for thermal conductivity. On the computational side, we also explore the effectiveness of the ancilla disentangler in the integrable and nonintegrable regimes of the model. We find that at high temperature, the disentangler helps by localizing the entanglement growth around the quench location allowing us to obtain the Drude weight in the integrable model. The improvement is insufficient to extract the asymptotic value of the correlator in the nonintegrable regime. The ancilla disentangler also provides no additional advantage at low temperatures.

DOI: 10.1103/PhysRevB.108.054304

I. INTRODUCTION

One-dimensional quantum systems host many experimentally realizable and theoretically tractable models that exhibit a rich set of quantum phenomena, including phase transitions, anomalous quantum transport, Luttinger liquids, etc. Transport setups that measure energy, spin or charge currents generated in response to weak external field gradients are widely used in characterization of such systems. Related questions of dynamics in weakly non-equilibrium situations have garnered considerable theoretical interest [1] and inspired the development of efficient algorithms [2–5] for their study. The spin-1/2 XXZ chain is an analytically tractable model that can be realized in certain one-dimensional quantum magnets [6,7]. Attempts to understand their measured transport properties led to many early works on isolated XXZ chains and closely related bosonic and fermionic models. These studies have revealed a connection between integrability and anomalous transport applicable not just in magnets but also in experimentally realizable bosonic and fermionic systems [8–11].

Based on the seminal works by Mazur and Suzuki which relate the value of time-averaged correlations with overlaps of operators and conserved charges [12,13], it was argued [14] that the conductivity of integrable systems such as the XXZ chain should have an anomalous zero frequency singularity (Drude weight). XXZ model is associated with two physically accessible conserved charges, namely energy and total spin quantum number along the z direction. The possibility of a finite Drude weight for thermal and spin conductivity, as well as broader features of associated transport, have been investigated in the XXZ model and its variants (including the cases with impurity [15,16] or noise [17]) over the past several decades [18–23].

In the gapless phase of the XXZ model, corresponding to the easy plane anisotropic case, early studies using Bethe ansatz suggested a finite zero temperature spin Drude weight which monotonically decreases with temperature [24]. The spin Drude weight decreases towards zero at all temperatures as the isotropic Heisenberg point is approached [25]. Numerical studies using exact diagonalization and a finite temperature generalization of the Kohn's formula [26–28] hints at vanishing spin Drude weight at finite temperatures in gapped phase when the system has net zero magnetization [29–32]. Results using generalized hydrodynamics and thermodynamic Bethe ansatz approach also indicate zero spin Drude weight in the gapped phase and finite spin Drude weight in the gapless phase [25]. Broadly the results also agree with time-dependent density matrix renormalization group (tDMRG) calculations which can access large finite size systems [20]. These results pertain to the zero magnetization ensembles; the spin Drude weight is finite in ensembles with finite magnetization even in the gapped phase [30]. Though the spin Drude weight has been found to be finite in the gapless phase, contrary to the expectation, the spin current operator is orthogonal to all local conserved charges obtained from the transfer matrix [14,33]. The finite Drude weight has been understood in terms of the Mazur bound related to the overlap of the spin current with certain additional quasilocal conserved charges [34,35].

The thermal current operator in the XXZ model is a conserved charge [14], and consequently the dynamical thermal conductivity has no finite frequency contribution. For the gapped phase, numerics and Bethe ansatz [14,36,37] approaches reveal a power-law decay of thermal Drude weight with temperature (T) at high temperatures and an exponential decay with $\frac{1}{T}$ at low temperatures, separated by a maximum at finite temperature. The trend is similar for the gapless regime, but the low temperature behavior [38] is linear in T there.

Besides the calculation of the Drude weight, other related aspects of ballistic transport have also been explored.

These include studies on Fourier's law violations in non equilibrium steady state currents generated in response to a potential gradient [2,15,16,39–43], studies of currents in ray-dependent steady states after quench from a bipartitioned system [44–50], and studies on the nature of spread of initial spin or energy packets [22,51–53]. Breaking the integrability in such models, for instance, by next nearest neighbor interactions or noise, results in vanishing of the Drude peak and transfer of the conductivity weight to finite frequencies [17,31,54–56].

While the XXZ model and equivalent fermionic and bosonic models have been explored in great detail, not much has been systematically explored in other models [57]. In this work, we investigate the $\mathbb{Z}_3$ chiral clock model with a spatial chirality [58–61]. The model hosts a rich phase diagram [62] and exhibits dynamics [44,63,64] of interest in Rydberg atom systems [65]. More importantly, for our current interest, the model is integrable in a certain part of the parameter space [66].

We numerically calculate the dynamical thermal conductivity in the integrable regime using techniques developed and applied successfully in the XXZ model and characterize the Drude weight as a function of the temperature and model parameters. The Drude weight is found to be finite at all finite temperatures and the temperature dependence qualitatively matches that of the thermal Drude weight in the XXZ model. We then borrow results on the transfer matrix of the classical chiral clock model [66] to construct local conserved charges for the quantum model. The Mazur bound from the simplest nontrivial charge $Q^{(2)}$ is found to saturate the numerically calculated Drude weight, which indicates that the current has a finite overlap only with $Q^{(2)}$. This allows us to obtain an asymptotically exact expression for Drude weight in the large temperature limit. The thermal current is not a conserved quantity, unlike the XXZ model and has a component that is not conserved and therefore orthogonal to all other conserved charges; we expect this to result in coexistence of diffusive and ballistic components in the dynamics of energy packets in this model.

In the past, several numerical techniques have been utilised to address the questions on transport phenomena in interacting quantum systems. Exact diagonalization techniques can estimate correlator of local observables with high accuracy but suffers from severe finite-size effect making the results unreliable in thermodynamic limit [30–32,67–70]. Tensor network based tDMRG method has also been used to investigate large system sizes and therefore, practically approaching thermodynamic limit with tunable error and computation cost [5,71]. A modified tDMRG approach based on the ancilla purification is found to be able to significantly reduce the computational cost of the simulation [20,72]. We use the latter in our calculation of the relevant correlators.

This paper is organized as follows. In Sec. II, we introduce the model. Next, in Sec. III, we present the expressions for the energy density and energy current; and introduce the relation between the conductivity and the current-current correlator which we use in the numerical calculations. We also discuss constraints satisfied by the thermal conductivity namely the sum rules and Kramers-Kronig like relation which we use in subsequent sections to validate our numerical results. We discuss the Mazur bound and the conserved charges in Sec. III D. Derivation of the conserved charges from the transfer matrix is presented in Appendix A. In Sec. IV, we outline the tDMRG method that was used to obtain the numerical results. Finally, in Sec. V, we present our key results including the Drude weights as a function of temperature and parameters and comparison with estimates from Mazur bound. This section also discusses the frequency content of the regular part of the dynamical thermal conductivity. In Sec. V D, we present our empirical observations regarding the efficiency of the ancilla disentangler used in tDMRG calculations and we conclude and summarize the results in Sec VI.

II. THE QUANTUM $\mathbb{Z}_3$ CHIRAL CLOCK MODEL

In this section, we introduce the $\mathbb{Z}_3$ symmetric quantum chiral clock model in one spatial dimension [58,60,61,73]. We assume open boundary conditions throughout unless mentioned otherwise. The model can be motivated as a generalization of the $\mathbb{Z}_2$ symmetric transverse-field Ising model [59]. The Hamiltonian is given by

$$H = -\sum_{j=1}^{L}[\bar{\alpha}_1\tau_j + \bar{\alpha}_2\tau_j^\dagger + \alpha_1\sigma_j\sigma_{j+1}^\dagger + \alpha_2\sigma_j^\dagger\sigma_{j+1}], \quad (1)$$

where the operators τ and σ satisfy the following algebra:

$$\tau^3 = \sigma^3 = \mathbb{I}; \quad \tau^\dagger = \tau^{-1}; \quad \sigma^\dagger = \sigma^{-1}; \quad \sigma\tau = \omega\tau\sigma,$$

and $\omega \equiv \exp(\frac{2\pi\iota}{3})$. These can be explicitly represented by the following matrices.

$$\sigma = \begin{pmatrix} 1 & 0 & 0 \\ 0 & \omega & 0 \\ 0 & 0 & \omega^2 \end{pmatrix}, \quad \tau = \begin{pmatrix} 0 & 0 & 1 \\ 1 & 0 & 0 \\ 0 & 1 & 0 \end{pmatrix}. \quad (2)$$

The algebra of the operators σ and τ generalizes that of the Pauli matrices S_z and S_x which appear in the Ising model.

The Hamiltonian is parameterized by complex scalar parameters α_1 and $\bar{\alpha}_1$, whose complex conjugates are denoted by α_2 and $\bar{\alpha}_2$, respectively. We emphasize that the bar does not indicate complex conjugates and the convention follows the one that has been used in literature [66].

Alternatively, we can use the following parametrization:

$$\alpha_1 = Je^{\iota\theta}, \quad \alpha_2 = Je^{-\iota\theta},$$
$$\bar{\alpha}_1 = fe^{\iota\phi}, \quad \bar{\alpha}_2 = fe^{-\iota\phi}, \quad (3)$$

where $f \geqslant 0$ is local Zeeman field and $J \geqslant 0$ is the nearest neighbor coupling. θ is a scalar parameter that governs the chirality. Nonzero ϕ breaks the time-reversal symmetry.

Depending on the parameters θ, ϕ, the model can have discrete symmetries, e.g., charge conjugation ($\sigma \leftrightarrow \sigma^\dagger, \tau \leftrightarrow \tau^\dagger$), spatial parity($j \leftrightarrow L - j + 1$) and time-reversal ($H \leftrightarrow H^*$) symmetry. In this work, we focus on $\theta \neq 0$ and $\phi = 0$ regime (i.e., $\bar{\alpha}_1 = \bar{\alpha}_2 = f \in \mathbb{R}$) where the model exhibits time-reversal symmetry. The model has a spatial chirality in this regime as the energy of left and right domain walls are not equal. The $\mathbb{Z}_3$ chiral clock model has a phase diagram with a disordered ($f \gg J$) phase and a $\mathbb{Z}_3$ symmetry broken ordered phase ($J \gg f$); the latter contains a topological regime [62,74,75]. The phases are separated by a surface of

second-order quantum phase transition points that passes through the critical point at $J = f$, $\theta = \phi = 0$ [76] for three state Potts model.

The model is integrable along the line [66]

$$f\cos(3\phi) = J\cos(3\theta) \tag{4}$$

and superintegrable when $\theta = \phi = \frac{\pi}{6}$ [77,78]. This work aims to understand aspects of the model along the integrable line. For simplicity, we consider only the parameter range where time reversal invariance holds and study the properties as θ varies keeping ϕ to be 0, leaving the calculations in the finite ϕ regime for a future work.

III. ENERGY DENSITY, THERMAL CURRENT OPERATOR AND DRUDE WEIGHT

A key signature of an integrable model is the nonzero Drude weight which refers to a zero frequency δ-function peak in the conductivity. In this work, we explicitly calculate the Drude weight in thermal conductivity as a function of temperature and Hamiltonian parameters. In the following subsections, we present the expressions for the energy density, thermal currents, conductivity, and its Drude weight.

A. Local energy density and thermal current operator

In order to calculate the Drude peak (and dynamical thermal conductivity in general), we study the two-point correlator for the thermal current whose definition depends on the choice of the form of the local energy density operator. We choose the local energy density as a three-site operator,

$$H_i = -\frac{\alpha_1}{2}(\sigma_{i-1}\sigma_i^\dagger + \sigma_i\sigma_{i+1}^\dagger) - \bar{\alpha}_1\tau_i + \text{h.c.} \tag{5}$$

The thermal current operator, I_i acting on the bond between site i and site $i+1$ can be inferred from continuity equation as $\dot{H}_i = \imath[H, H_i] = -\{I_{i+1} - I_i\}$. The local current operator I_i has the form

$$I_i = \imath\frac{\bar{\alpha}\alpha_1}{2}\left(I_i^{(1)} + I_i^{(2)}\right) + \text{h.c.}, \tag{6}$$

where

$$\begin{aligned} I_i^{(1)} &= (\omega^2 - 1)\sigma_i(\tau_i + \tau_{i+1})\sigma_{i+1}^\dagger, \\ I_i^{(2)} &= (\omega - 1)\sigma_i(\tau_i^\dagger + \tau_{i+1}^\dagger)\sigma_{i+1}^\dagger. \end{aligned} \tag{7}$$

The total current operator is defined as $I = \sum_{i=1}^{L} I_i$. Symmetry considerations imply that the current operator has zero expectation value in any thermal state [43].

B. Thermal conductivity and sum rule

Fourier transform of thermal conductivity in the linear response regime is given by [79,80]

$$\kappa(k, \Omega_+) = \lim_{L\to\infty}\frac{1}{\hbar T k L}\int_{-\infty}^{0} e^{-\imath\Omega_+ t}\langle[\hat{I}(k,0), \hat{H}(-k,t)]\rangle\,\mathrm{d}t, \tag{8}$$

where operators with hat ($\hat{I}$ and $\hat{H}$) represent the corresponding spatial Fourier transformed form, $\Omega_+ = \Omega + \imath 0^+$, T is temperature (in unit of J), L is the number of sites. Integrating Eq. (8) by parts and subsequently using continuity equation and the Kubo-Martin-Schwinger (KMS) condition [81] on the resulting expression, the thermal conductivity in the long wavelength limit ($k \to 0$) reduces to

$$\kappa(\Omega) = \frac{1 - e^{-\beta\Omega}}{T\Omega}\int_0^\infty e^{\imath\Omega t}\lim_{L\to\infty}\frac{\langle I(t)I(0)\rangle}{L}\,\mathrm{d}t, \tag{9}$$

which can be used to numerically evaluate the thermal conductivity (hereafter we use thermal conductivity to refer to its long wavelength limit only). The current-current correlator is directly accessible in the numerical time evolution which we implement using finite temperature tDMRG methods [4,20,45,52,71,82].

As shown in Ref. [83], thermal conductivity satisfies the following sum rule:

$$\int_0^\infty \mathrm{Re}\,\kappa(\Omega)\,\mathrm{d}\Omega = \lim_{L\to\infty}\frac{\pi}{2\hbar T L}\langle\Theta\rangle, \tag{10}$$

which we can use to validate the numerically estimated conductivity. We set $\hbar = 1$ throughout this work. Here Θ is called the thermal operator for which an exact expression is given by

$$\Theta = -\lim_{k\to 0}\frac{\mathrm{d}}{\mathrm{d}k}[\hat{I}(k), \hat{H}(-k)]. \tag{11}$$

The expectation value in Eq. (10) is calculated in the thermal ensemble. For the specific choice of current and energy operator, Θ can be expressed in terms of local real space operators as follows:

$$\Theta = \frac{\imath}{2}\sum_i [I_i, -3H_{i-1} - H_i + H_{i+1} + 3H_{i+2}]. \tag{12}$$

C. Drude weight

The extensive number of conservation laws in the integrable model can result in a nonzero value for the current-current correlator at asymptotically large time, resulting in a divergent zero frequency contribution to the thermal conductivity. The real part of conductivity in the Fourier space has the following decomposition:

$$Re\,\kappa(\Omega) = 2\pi D_{\text{th}}\delta(\Omega) + \kappa_{\text{reg}}(\Omega), \tag{13}$$

where

$$\begin{aligned} D_{\text{th}}(T) &= \lim_{t\to\infty}\lim_{L\to\infty}\frac{\langle I(t)I(0)\rangle}{2LT^2} \\ &= \lim_{t\to\infty}\lim_{L\to\infty}\frac{\langle I(t)I_{L/2}(0)\rangle}{2T^2}. \end{aligned} \tag{14}$$

We have invoked spatial translation invariance in the second equality. This can be directly evaluated in tDMRG calculations.

As shown in Ref. [72], thermal conductivity can be calculated from the real or the imaginary part of the current-current correlator; and the difference between the two can be used as an estimate of the error in the calculated thermal conductivity. First, the real regular part of the dynamical thermal conductivity [Eq. (13)] can be obtained directly from Eq. (9). Moreover,

thermal conductivity Re $\kappa_{\rm reg}(\Omega)$ can also be estimated using

$$\text{Re}\,\kappa_{\rm reg}(\Omega) = -\frac{2}{T\Omega}\text{Im}\int_0^\infty e^{\iota\Omega t}\,\text{Im}\left[\lim_{L\to\infty}\frac{\langle I(t)I(0)\rangle_{\rm reg}}{L}\right]\text{d}t, \tag{15}$$

where $\langle I(t)I(0)\rangle_{\rm reg}$ is obtained from $\langle I(t)I(0)\rangle$ by subtracting $\langle I(t)I(0)\rangle_{t\to\infty}$ from $\langle I(t)I(0)\rangle$. In addition to the sum rule, discussed in the previous section, we use this to estimate error in the calculated regular part of thermal conductivity (See Appendix D).

D. Mazur bound

The Drude weight is related to conserved charges of the integrable model through Mazur's inequality [12,13]. Assuming that the correlator has a steady asymptotic value, we can express this as the long time average of current-current correlator expectation value. For averages over a sufficiently large time window, the fluctuating contributions vanish from the spectral expansion, and we get [84]

$$\lim_{\Lambda\to\infty}\frac{1}{\Lambda}\int_0^\Lambda dt\,\langle I(t)I(0)\rangle \;=\; \sum_{\substack{m,n\\ E_n=E_m}}\frac{e^{-\beta E_n}}{Z}|\langle n|I|m\rangle|^2, \tag{16}$$

where $Z=\text{Tr}[\rho]$, $\rho=e^{-\beta H}$ and E_m denotes the energy of the $m^{\rm th}$ eigenstate, $|m\rangle$ and $\beta=\frac{1}{T}$ is the inverse temperature.

We denote the extensive set of Hermitian local conserved charges by $\{Q^{(j)}:[Q^{(j)},H]=0\}$. The conserved charges can always be made orthogonal (under the operator inner product $\langle A,B\rangle_\rho=\text{Tr}[\rho A^\dagger B]$) i.e., $\langle Q^{(j)},Q^{(k)}\rangle\propto\delta_{jk}$.

Any operator that is diagonal in the energy basis must be a conserved charge for the Hamiltonian. This implies in particular that the diagonal part of current operator, I is a constant of motion. Consequently, the total current operator, I can be expanded as

$$I=\sum_{k=1}a_kQ^{(k)}+I', \tag{17}$$

where

$$a_k=\frac{\langle Q^{(k)},I\rangle_\rho}{\langle Q^{(k)},Q^{(k)}\rangle_\rho}$$

and I' is a purely off-diagonal matrix in any energy eigenbasis, i.e., $\langle m|I'|n\rangle=0$ if $E_m=E_n$. Using the expression for I from Eq. (17) in Eq. (16), we obtain the following expression for the asymptotic value for the current-current correlator

$$\lim_{\Lambda\to\infty}\frac{1}{\Lambda}\int_0^\Lambda \text{d}t\,\langle I(t)I(0)\rangle=\sum_k\frac{|\langle Q^{(k)},I\rangle_\rho|^2}{\langle Q^{(k)},Q^{(k)}\rangle_\rho}, \tag{18}$$

where sum is over conserved charges. Equation (18) can be used to get the following expression for the Drude weight in terms of overlap of current operator and conserved charges:

$$D_{\rm th}(T)=\lim_{L\to\infty}\frac{1}{2LT^2}\sum_k\frac{|\langle Q^{(k)},I\rangle_\rho|^2}{\langle Q^{(k)},Q^{(k)}\rangle_\rho}. \tag{19}$$

The right-hand side is a sum of non-negative terms, and in the absence of a complete set of conserved charges the expression still provides a lower bound on the Drude weight.

There exists a one parameter family of 3^L dimensional transfer matrices $\mathbb{T}(u)$ [66,85] parametrized by u for the classical chiral Clock model in periodic boundary condition. For parameters that satisfy Eq. (4), $\mathbb{T}$ commutes with the quantum Hamiltonian as well as with each other (i.e., $[\mathbb{T}(u),\mathbb{T}(u')]=0$).

An extensive number of local conserved charges for the quantum model can be obtained from a formal Taylor expansion of $\ln(\mathbb{T})$ in powers of u (see for instance Ref [86]):

$$\ln\mathbb{T}(u)=\sum_{j=1}^\infty Q^{(j)}u^j. \tag{20}$$

The simplest conserved charge $Q^{(1)}$ is the quantum Hamiltonian. The next term in the expansion namely $Q^{(2)}$ is a three- local conserved charge with the following form (See Appendix A for details):

$$\begin{aligned}Q^{(2)}=&\sum_k I_k+\iota\left(\frac{1}{2}+\omega\right)\left(\frac{\alpha_1^2\bar\alpha}{\alpha_2}-\bar\alpha^2\right)\tau_k\\&+\iota\left(\frac{1}{2}+\omega^2\right)\left(\frac{\alpha_1^2\bar\alpha}{\alpha_2}-\bar\alpha^2\right)\tau_k^\dagger.\end{aligned} \tag{21}$$

The expression for $Q^{(3)}$ is presented in Appendix A.

The thermal current has a finite overlap with $Q^{(2)}$ and zero overlap with $Q^{(1)}$ and $Q^{(3)}$; this can be explicitly computed for the infinite temperature ensemble, and numerically observed to hold at all finite temperatures. This is similar to the case of the XXZ model [14]. Further, the numerical results in the subsequent sections show that the thermal current has a finite overlap only with $Q^{(2)}$ as the bound on the Drude weight calculated from only $Q^{(2)}$ using Eq. (19) saturates the Drude weight calculated from asymptotic value of the finite temperature current-current correlator. However, unlike the XXZ model, the thermal current is not a conserved quantity in itself and $Q^{(2)}$ is not proportional the current. Only at critical point ($\alpha_1=\alpha_2=\bar\alpha$), conserved charge $Q^{(2)}$ coincide with the thermal current operator [Eq. (21)].

IV. NUMERICAL METHOD

To calculate the dynamical current-current correlator in Eq. (14), we employ a time-dependent DMRG method (tDMRG) implemented using matrix product states. We realize the finite temperature system as the subsystem of a bigger system containing the L physical and L ancilla degrees of freedom in a pure entangled state ψ_β such that reduced density matrix of the physical degrees of freedom is $e^{-\beta H_{\rm phy}}/Z$ [87]. $H_{\rm phy}$ is the Hamiltonian in Eq. (1) applied only on the subsystem of physical sites. To prepare the state ψ_β we start with a state where each physical site is maximally entangled with one neighboring ancilla, representing the purification ψ_0 of an infinite temperature physical system. The purification of the physical system at inverse temperature β is obtained through an imaginary time evolution of the initial state: $|\psi_\beta\rangle\propto e^{-\frac{\beta}{2}H_{\rm phy}}\otimes\mathbb{1}_{\rm anc}|\psi_0\rangle$. Both imaginary and subsequent real time evolutions are implemented through a fourth-order Trotter decomposition [5].

To slow down the bond dimension growth and access the largest possible time scale, we exploit the fact that purification

is not unique as outlined in Ref. [20], due to the invariance of the reduced density matrix of the physical system under arbitrary unitary transformations of the ancilla subsystem. Entanglement growth can be slowed down by applying a suitable disentangler unitary on the ancilla subsystem. For XXZ model, $U = \mathbb{I}_{\text{phys}} \otimes e^{+\iota H_{\text{anc}} t}$ where H_{anc} is the same as the Hamiltonian for the physical system (H_{phy}) but, acting instead on the ancilla subsystem only (See Refs. [20,82,88] for details).

In this model [Eq. (1)] as well, we observe empirically that, within a restricted class of unitaries considered, the above unitary is optimal (See Appendix C). This particular choice of U_{anc} makes the time evolution of thermal state $|\psi_\beta\rangle$ nearly trivial, and for the quenched state (the thermal state perturbed by the operator, i.e., $I_{L/2}|\psi_\beta\rangle$ in the present case), entanglement buildup gets confined in the vicinity of the site where the current operator is applied. We found that for our calculations, it was sufficient to use a maximum bond dimension of χ of 900–1200 and a singular value cutoff (ϵ) of $10^{-9} - 10^{-12}$ for truncation to get results with sufficient convergence. We repeated the calculation for multiple system sizes, cut-off bond dimensions (χ) and truncation weight cutoffs (ϵ) to confirm the convergence of our results (See Appendix B).

One further optimization often carried out in such numerical calculations of correlator is to exploit the time translation invariance in correlator where we write $\langle A(t)B(0)\rangle$ as $\langle A(-t/2)B(t/2)\rangle$ [89]. Unlike the case for the two-point correlator between a pair of *local* observables, we have a task of evaluating a correlator of the form $\langle I(t)I_{\frac{L}{2}}(0)\rangle$ where one of the two operators is a *sum of local* observables. The alternate strategy of calculating the required correlator as the sum of correlators of local objects $\langle I_i(t/2)I_{\frac{L}{2}}(-t/2)\rangle$ has a cost that is typically higher [89,90].

All the numerical calculations in the following section were carried out using code built on ITensor [91,92].

V. NUMERICAL RESULTS

In this section, we present the results from the numerical calculations using methods discussed in the previous section. All the results presented in the main text are for a system of $L = 60$ physical sites. The time step for tDMRG evolution is 0.05. This section is organized as follows. The general features of the dynamical current-current correlations and thermal conductivity are presented in Sec. V A and verification of the sum rule is discussed in Sec. V B. The main results of the work, namely the variation of Drude weight with temperature and parameters, as well as a comparison with the Mazur bound are described in Sec. V C. Lastly, we present an analysis of the efficiency of the disentangler unitary that we chose in Sec. V D. Except in the last subsection, we consider only the integrable line, along which the chirality θ is fixed by the integrability condition Eq. (4); as f increases from 0 to 1, θ decreases from $\pi/6$ to 0.

A. Current-current correlator and thermal conductivity

Figure 1(a) shows the time dependence of the real part of the current-current correlator for a range of temperatures at a fixed Hamiltonian parameter $f = 2/5$. The black dotted lines show the estimates from the Mazur bound Eq. (18). The calculated asymptotic value of current-current correlator is in excellent agreement with the Mazur bound. Generally, the time taken to reach the asymptotic value is longer at lower temperatures. Time dependence of the real part of the current-current correlator at a fixed temperature $T = 5$ and different points along the integrable line is shown in Fig. 1(b). Note that in the time series plot shown in Figs. 1(a) and 1(b) or the Fourier transforms presented below, we have not used any extrapolation on the time series data [93] obtained from tDMRG. All the data shown are from the actual tDMRG evolution. We did not find any qualitative changes to the results upon using the extrapolated data.

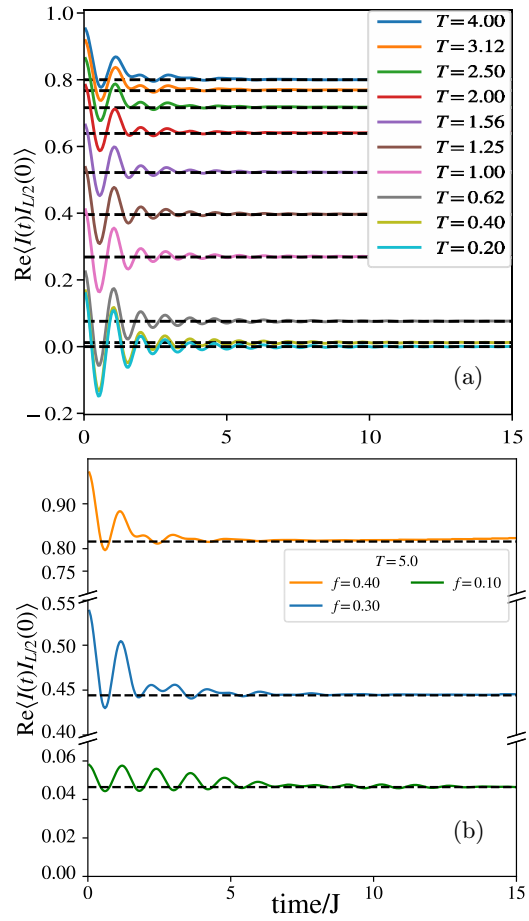

FIG. 1. (a) Evolution of the current-current correlator. The black dotted lines are lower bound on asymptotic value of current-current correlator at different temperatures obtained from Mazur bound. The maximum bond dimension for MPS is kept at 900–1200 with a cutoff for truncation $\sim 10^{-9} - 10^{-12}$. $J = 1$, $f = 2/5$, $\theta = \frac{1}{3}\cos^{-1}(2/5)$. (b) Evolution of the current-current correlator for different f along the integrable line at $T = 5$. Cutoff for truncation, $\epsilon \sim 10^{-9} - 10^{-12}$.

Fourier transform of the conductivity can be calculated from the current-current correlator using Eq. (9). Figure 2(a) shows the variation of the regular part of the thermal conductivity as a function of Ω across a range of Hamiltonian parameter f. The 0 frequency contribution is not shown in the plot. As f increases from 0 to 1 (simultaneously θ varies from $\pi/6$ to 0 along the integrable line), the peak broadens but, for f close to 1 the peak rapidly decreases in height and vanishes

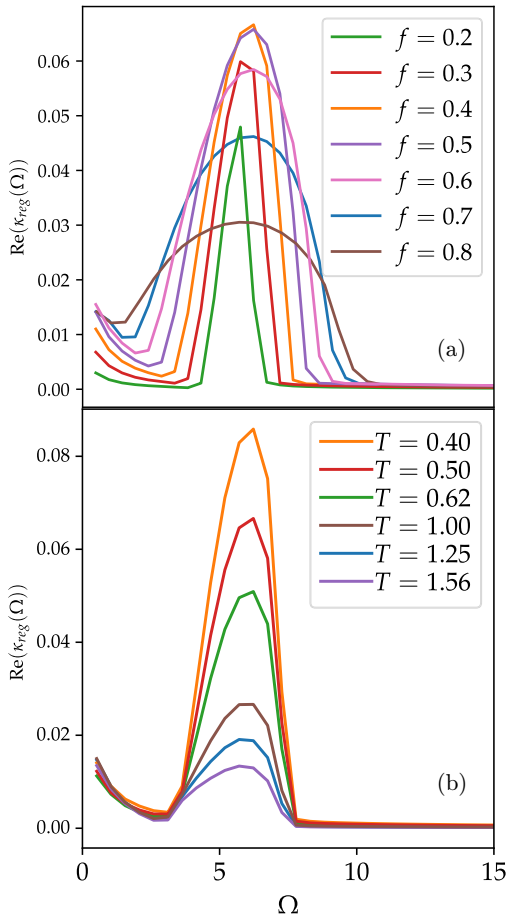

FIG. 2. (a) Real part of Fourier transformed regular thermal conductivity $T = 0.5$ as a function of Ω. Different lines correspond to different values of Hamiltonian parameter f along the integrable line. (b) Similar to (a) but for different values of temperature (T). Results shown are for $J = 1$, $f = 2/5$, $\theta = \frac{1}{3}\cos^{-1}(2/5)$, $\phi = 0$.

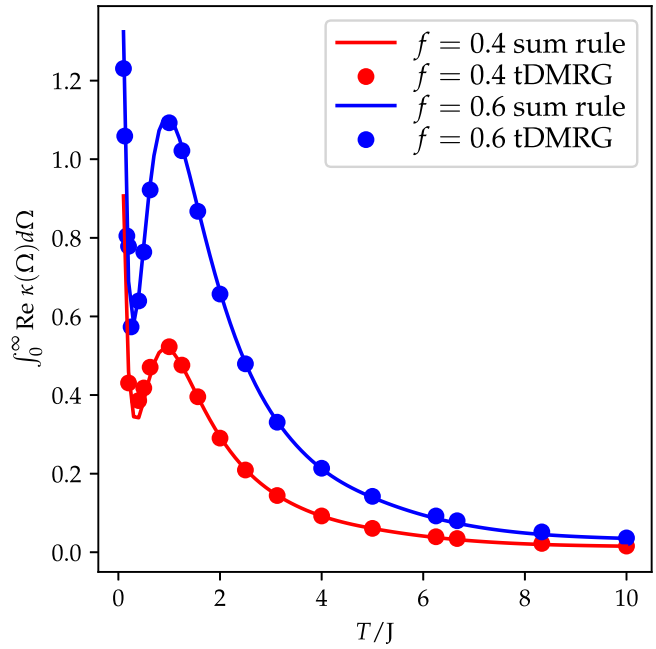

FIG. 3. Verification of the sum rule by comparing RHS of Eq. (10) (solid line) where the expectation value of Θ is calculated numerically using Eq. (12). The dots indicate the integral of real part of Eq. (9) obtained from real time correlatlor $\langle I(t)I_{\frac{L}{2}}\rangle$ evaluated using tDMRG. The different lines show results for different points on the integrable line.

at $f = 1$. In particular the κ_{reg} is exactly 0 for all frequencies at the critical Potts model point ($f = 1, \theta = 0, \phi = 0$).

$\kappa(\Omega)$ has a δ-function peak arising from the Drude weight, the remaining regular part κ_{reg} of the conductivity as a function of the frequency is shown in Fig. 2(b). κ_{reg} is near zero at the highest accessible frequency and is finite for $\Omega \to 0$. This finite DC value indicates a finite diffusive part ($\propto T\kappa_{\mathrm{reg}}(\Omega \to 0)$) in the energy transport in addition to the ballistic part. In the gapped phase of the XXZ model, when the spin Drude weight is 0, the regular part of the conductivity has a large finite peak as $\Omega \to 0$. This appears to diverge at zero temperature [72] qualitatively consistent with the semiclassical model proposed in Refs. [94,95]. Due to errors arising from finite time data (See Appendix D), we cannot detect the temperature dependence of $\kappa_{\mathrm{reg}}(\Omega \to 0)$ reliably. At an intermediate range of frequencies (3.0 to 7.5 in this case) there is a finite peak whose height decreases with increasing temperature. This frequency range is independent of the temperature.

Now we consider the location of the peak in relation to the spectral gap. For the value of f considered in Fig. 2, the gap above the ground state is $\Delta = 1.2551$ (calculated using DMRG in a system of size 60). This should correspond to the lowest energy domain wall quasiparticle. Energy of the domain wall with the opposite chirality should be higher due to finite chirality θ [63]. Insertion of the current operator $I_{L/2}$ is expected to generate a pair of opposite chirality domain walls (τ operators in Eq. (7) flips a single spin, generating a pair of domain walls around it) whose energy should be more than $\sim 2\Delta$ consistent with the low-frequency end Ω_{low} of the peak. An alternate possibility is that a chain of three domain walls $|...11...\omega\omega...\omega^2\omega^2...11...\rangle$ of same chirality costing an energy of $\sim 3\Delta$ determines the location of low-frequency end. Within the resolution possible for Ω_{low}, the two scenarios cannot be distinguished. As the critical point is approached, $f \to 1, \theta \to 0$, the spectral gap vanishes, which is consistent with vanishing Ω_{low} in Fig. 2(a).

B. Sum rule

We now verify the sum rule for thermal conductivity following Eq. (10). Figure 3 shows the integrated value of (numerically calculated) real part of thermal conductivity, Re $\kappa(\Omega)$ (LHS of Eq. (10) shown as dots in the figure) compared with the expected sum (RHS of Eq. (10) shown as continuous lines) as a function of temperature. We find good agreement between the two, implementing a partial check on the current-current correlator calculated numerically.

The T in the denominator of Eq. (10) results in a spike at low temperature in Fig. 3. The sharp increase in integrated thermal conductivity at low temperature arises from the intermediate frequency peak in Fig. 2 that gets more significant at low temperatures. The finite temperature peak in the sum rule arises from the singular, zero frequency part, i.e., Drude

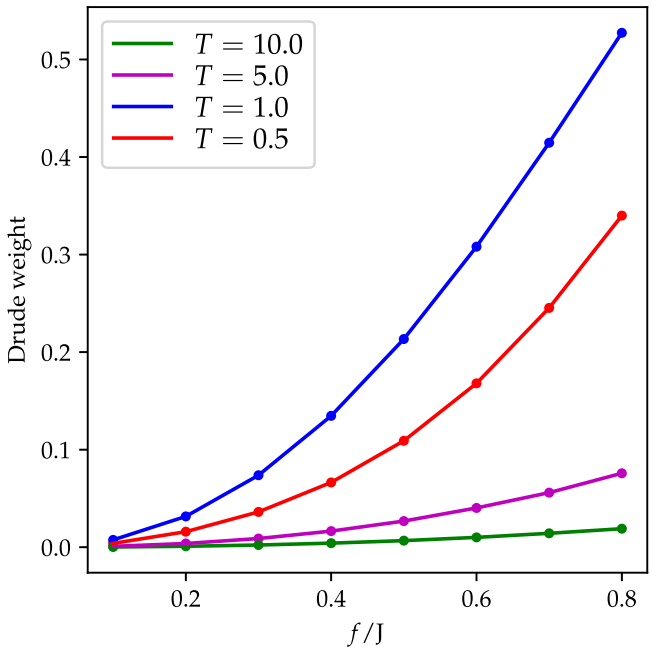

FIG. 4. Drude weight calculated from tDMRG as a function of f showing the monotonic increase of Drude weight with increasing f. θ is chosen accoding to f along integrable line. The solid line is a linear interpolation between data shown as a guide to the eye.

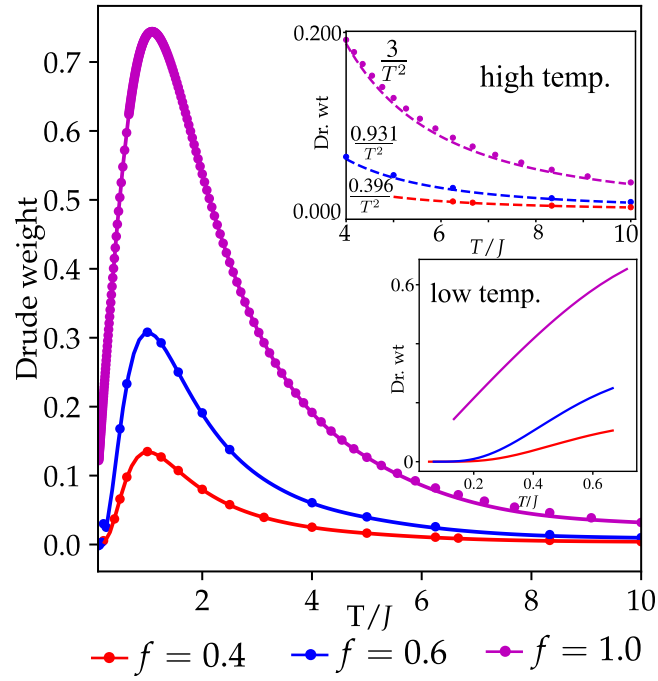

FIG. 5. Variation of the Drude weight with temperature for different values of f. The solid lines show the Mazur bound Eq. (19). Dot markers show the Drude weight estimated from tDMRG data Eq. (14). Temperature axis starts from $T = 0.1$. (Inset) High temp: Asymptotic expression for Drude weight is represented by the dashed lines Eq. (22). The dots are from tDMRG estimates. Low temp: Drude weight from Mazur Bound in the low temperature regime. Behavior for the critical point is consistent with a linear scaling with T while for the gapped phase the trend is consistent with $e^{-\frac{\delta}{T}}$.

weight of the thermal conductivity. Fig. 3 has a similar trend as in Fig. 5 at intermediate and high temperature.

C. Variation of Drude weight with temperature and Hamiltonian parameters

In this section, we present the results for the numerically calculated Drude weights as a function of the temperature and comparison with the Mazur bound. Figure 4 shows the Drude weight computed from tDMRG as a function of the f for different temperatures showing a monotonic (nearly quadratic at small f) increase with f. Drude weight changes non-monotonically with temperature as can be inferred from comparing the plots for $T = 0.5, 1, 5.0$.

Figure 5 shows the Drude weight numerically computed using tDMRG (dots in the figure) as a function of temperature for different values of f; and as mentioned before, the temperature dependence is nonmonotonic. The solid lines show the Mazur bound calculated numerically using Eq. (19) considering only the $Q^{(2)}$ charge (See discussion in Sec. III C and Appendix A). The Mazur bound from $Q^{(2)}$ saturates the estimated Drude weight indicating that the thermal current has no overlap with any other conserved charge.

Drude weight tends to zero at zero temperature and increases rapidly as temperature is increased till it reaches a finite temperature peak around $T = 1$. The high temperature asymptotic behavior of the Mazur bound from charge $Q^{(2)}$ can be estimated to be

$$D_{\text{th}}(T = \infty) = \frac{1}{2T^2} \frac{\langle I, Q_i^{(2)} \rangle_{\rho=\mathbb{I}}}{\langle Q_i^{(2)}, Q_i^{(2)} \rangle_{\rho=\mathbb{I}}} = \frac{1}{2T^2} \frac{24f^2}{5 - f^2}. \quad (22)$$

For $f \ll 1$, the above expression suggests a quadratic variation with f consistent with Fig. 4. Figure 5 (inset: high temp) shows the agreement (asymptotically) of Eq. (22) with data obtained from tDMRG at high temperature.

In the low temperature (inset: low temp) regime, Drude weight decays linearly with T for the critical system. The behavior is qualitatively different in the gapped system ($f \neq 1$), where we observe a decay to 0 as $e^{-\frac{\delta}{T}}$. We can extract δ by fitting this to our data. For the two cases we considered here, $f = 0.4$ and 0.6, we find $\delta \sim 1.19$ and 0.98, which are close to the corresponding spectral gap of 1.25 and 0.95 above the ground state, respectively.

D. Efficiency analysis of the tDMRG with ancilla disentangler

The results presented in the previous sections were achieved using a disentangler unitary (See Sec. IV) on the ancilla subsystem in the tDMRG calculations. The disentangler slows entanglement growth in general and makes accessing longer time scales possible. The effectiveness of this approach however, varies with the parameter and temperature regimes; qualitatively similar to what was found in the case of XXZ model [82]. In this section, we present our empirical observations along with some quantitative data on the efficacy of the disentangler approach across model parameters and temperature for the model studied here.

In Figs. 6(a) and 6(b) we show the variation of the maximum bond dimension after time evolution of the quenched ($I_{\frac{L}{2}}|\psi_\beta\rangle$) and thermal ($|\psi_\beta\rangle$) states, respectively. In each case,

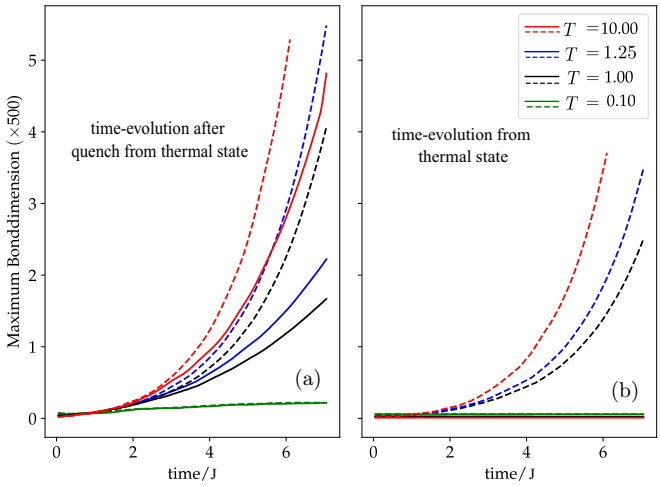

FIG. 6. (a) Growth of maximum bond dimension under real time evolution for the matrix product state (MPS) quenched from thermal state at different values of β. The dotted line indicates tDMRG without application of disentangler and the solid line is for disentangled tDMRG. (b) Same as panel (a) but, for time evolution of thermal MPS without any quench. The parameters for the Hamiltonian are $J = 1$, $f = 2/5$, $\theta = \frac{1}{3}\cos^{-1}(2/5)$, $\phi = 0$ (integrable point). The truncation cutoff,$\epsilon = 10^{-9}$.

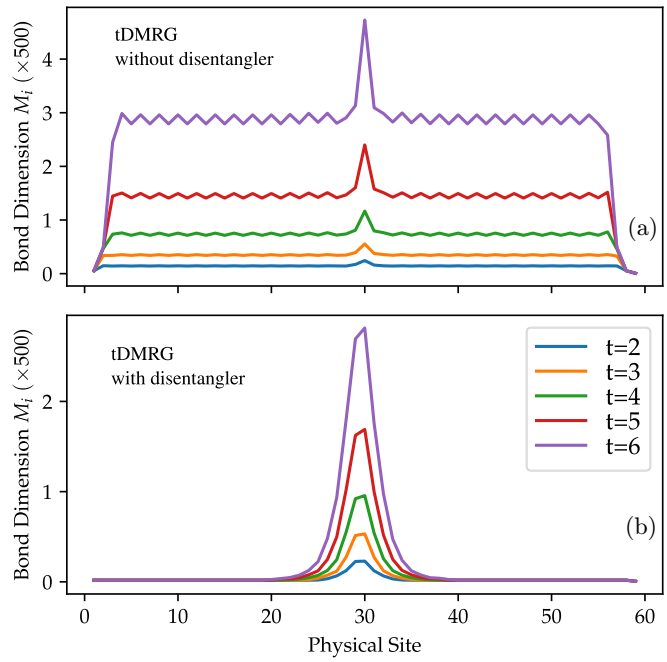

FIG. 7. Bond dimension as a function of bond position for the state quenched from a high temperature ($T = 6.25J$) thermal state. (a) data for tDMRG without disentangler and panel (b) shows data for tDMRG with disentangler. Different lines correspond to different times. The MPS bond dimension growth is localized about the quench site in case of tDMRG with disentangler. Results shown are for the integrable point $J = 1$, $f = 2/5$, $\theta = \frac{1}{3}\cos^{-1}(2/5)$, $\phi = 0$. The truncation cutoff, $\epsilon = 10^{-9}$.

we compare the bond-dimension growth with and without disentanglers applied to the ancilla. From Fig. 6(a), we observe that the maximum bond dimension of the quenched matrix product state (MPS) grows much faster (up to 2.5 times) for tDMRG without disentangler (dotted line) in contrast to the tDMRG with disentangler (solid line). At low temperatures, on the other hand, both methods show almost similar growth in maximum bond dimension with time. In Fig. 6(b), we see that the tDMRG with disentangler almost fully eliminates bond dimension growth of the thermal MPS under unitary evolution. In contrast, unitary evolution of thermal MPS ($|\psi_\beta\rangle$) implemented using tDMRG without disentangler shows rapid growth of maximum bond dimension with time.

In Fig. 7, we show the bond dimension of the time evolved states, as a function of the bond position contrasting the cases of real-time evolution with and without disentangler. We notice a uniform growth of bond dimension throughout the system in the state that evolved without the ancilla disentangler in contrast to localized growth of bond dimensions near the quench site in case of tDMRG with disentangler. The spatial support of the operator is expected to spread linearly with time evolution; this increase is manifested in the excess growth of entanglement around the quench site (center in our case). Without disentangler, however, there is an additional uniform buildup of entanglement everywhere in the system. In Fig. 8, we show local bond dimension at low temperature. Here, in both cases (tDMRG with and without disentangler unitary), local bond dimension shows similar behavior indicating no significant gain in efficiency from the application of ancilla disentangler.

We, so far, focused on the local bond dimension growth. However, time evolution calculations are dominated by matrix multiplications and singular value decomposition (SVD) operations with a computational complexity of $O(d^3)$ where d

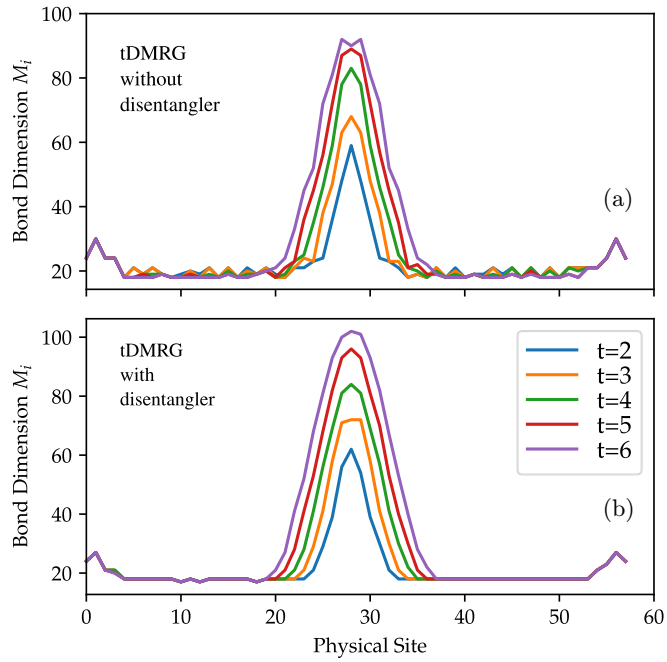

FIG. 8. Similar to Fig. 7, this plot shows the spatial distribution of bond dimension but at a low temperature point $T = 0.1$ (in unit of J). The parameters for Hamiltonian are $J = 1$, $f = 2/5$, $\theta = \frac{1}{3}\cos^{-1}(2/5)$, $\phi = 0$. The truncation cutoff is $\epsilon = 10^{-9}$.

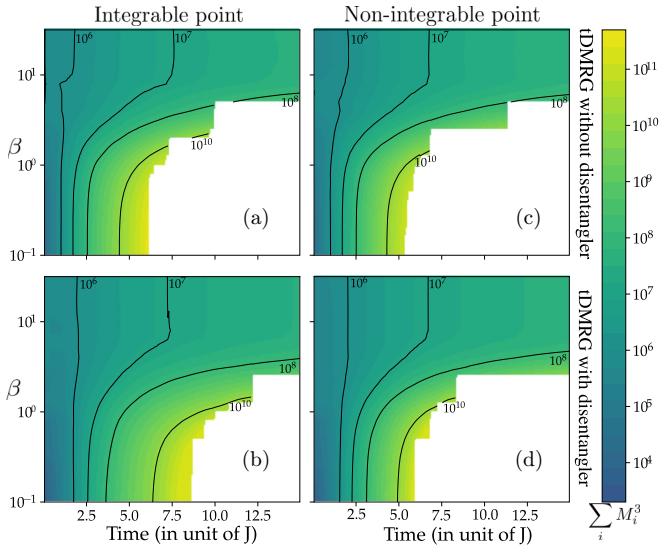

FIG. 9. Computational complexity as a function of β and time. (a) and (b) are for integrable model ($J = 1$, $f = 2/5$, $\theta = \frac{1}{3}\cos^{-1}(2/5)$, $\phi = 0$) with and without disentangler unitary, respectively. (c) and (d) are for nonintegrable point $J = 1$, $f = 2/5$, $\theta = 0.3$, $\phi = 0$ with and without disentangler unitary, respectively. Colors indicate a measure of the computational cost. Contour lines connect points of same computational cost. The truncation cutoff was maintained at $\epsilon = 10^{-9}$ throughout the calculations.

is the dimension of the matrices involved. Denoting the local bond dimension at site i of the MPS by M_i, the computational cost can be quantified by $\sum_i M_i^3$ [82]. In Fig. 9, we provide a contour plot showing the variation of the computational cost $\sum_i M_i^3$ with inverse temperature β and time, while keeping the truncation cutoff fixed at 10^{-9}.

We first compare Figs. 9(a) and 9(b) where, we show the contour plot for integrable points. We observe that the tDMRG with disentangler affords us an improvement in the accessible time scale — the same computational cost (the contour lines) is reached at a later time if the disentangler is applied, as compared to the case without the disentangler. However, the improvement is most significant at higher temperatures, where the bond dimensions growth is generally much faster and is, therefore, a relevant consideration. At low temperature where the bond dimension growth is a lesser issue, the disentangler performs slightly worse. These observations are consistent with Fig. 7 and Fig. 8.

Finally, we discuss Figs. 9(c) and 9(d) where we study a nonintegrable point. The plots suggest a minor gain in accessible time scales from ancilla disentangler. However, at nonintegrable points, we find that the time scales required for the transients in the current-current correlator to decay away is much larger compared to the integrable points; the improvements afforded by the disentangler is not sufficient for us to reach these time scales.

VI. SUMMARY AND OUTLOOK

The constraints imposed by the extensive number of local conservation laws in integrable systems manifest in many different ways, such as failure to thermalize to a Gibbs ensemble, long-term memory of initial states which strongly influence equilibrium steady state properties, unusual features in energy spectral correlations, and anomalous signatures in measurable long-time response functions such as conductivity. The precise relation between these features has been extensively investigated in the past several decades. This study uses extensive tDMRG calculations to characterize the anomalous zero frequency peak parametrized by the thermal Drude weight at integrable points of the $\mathbb{Z}_3$ chiral clock model, extending the features observed through past studies in the XXZ model.

The thermal Drude weight is nonzero at all finite temperatures. It vanishes as a power law $\sim 1/T^2$ at large temperatures and appears to decay exponentially with $1/T$ at low temperatures. At the critical point, the low-temperature Drude weight fits a linear behavior with T till the lowest temperature we studied ($T = 0.1$). These observations are consistent with what was observed in the gapped and gapless phases of the XXZ model.

The numerically obtained Drude weights (from current-current correlator) show excellent agreement with the Mazur bound based on the simplest nontrivial conserved charge $Q^{(2)}$ [Eq. (21)] derived from the transfer matrix and suggests that the thermal current has finite overlap only with one conserved charge. Consistent with this, explicit calculations show that the next order conserved charge $Q^{(3)}$ is orthogonal to the current.

The thermal current operator is however not identical to the conserved charge $Q^{(2)}$. This corresponds to a scenario where part of the energy current is conserved, manifesting as the finite Drude weight. The difference between the current and the conserved charge results in a nontrivial finite frequency part to κ_{reg}. This is unlike the case of the XXZ model, where the thermal current is a conserved charge and $\kappa_{\text{reg}} = 0$.

The regular part of the dynamical conductivity shows a broad peak at frequencies which could be correlated with the energies of the simplest domain walls. We also find a small finite conductivity near zero frequency, suggesting the possibility of a diffusive component to the energy transport in addition to the ballistic part.

We used the ancilla disentangler to increase the maximum times up to which we could compute the correlator. For the integrable points, this allowed us to efficiently access the asymptotically long-time behavior of the correlator. However, for the nonintegrable points we checked, the improvement afforded by the method was insufficient to access features of the correlators at sufficiently long times to see the asymptotic behavior. More careful choice of the nonintegrable parameter regime, use of other disentangler schemes [88], alternate computing schemes [96] or truncation methods [97,98] may help access longer time scales.

In this work, we have characterized the anomalous transport properties at the chiral but time-reversal invariant points in the integrable parameter space of the model. The similarities of our results with the XXZ model highlights the universality of the relation between integrability and anomalous transport, and suggests similar qualitative features for the time reversal broken ($\phi \neq 0$) regime as well. However it will be interesting to understand how broken time-reversal invariance manifests in the anomalous transport features. The model also provides an interesting arena to study dynamics

and transport at superintegrable [77,78] points and effects of integrability breaking perturbations on them.

ACKNOWLEDGMENTS

We thank R. Sensarma and T. Sadhu for useful discussions and K. Damle and P. Fendley for clarifications on previous works. We are grateful to D. Dhar for pointing us to Ref. [86]. S.G.J. thanks S. Kundu for help with accessing missing figures of Ref [86]. S.G.J. acknowledges Tata Institute for Fundamental Research, Mumbai for their hospitality during the completion of this work. We also thank National Supercomputing Mission (NSM) for providing computing resources of PARAM Brahma at IISER Pune, which is implemented by C-DAC and supported by the Ministry of Electronics and Information Technology (MeitY) and Department of Science and Technology (DST), Government of India. S.G.J. acknowledges support from the National Mission on Interdisciplinary Cyber-Physical Systems (NM-ICPS) of the Department of Science and Technology, Govt. Of India through the I-HUB Quantum Technology Foundation.

APPENDIX A: TRANSFER MATRIX AND CONSERVED CHARGES

In this section, we give an outline for the derivation of the conserved charges of quantum $\mathbb{Z}_3$ chiral clock model from the transfer matrix for a classical 2D chiral clock model. Here we borrow the results for the transfer matrix from Ref. [66].

The energy density of the classical 2D model is [60]

$$\mathcal{E} = -2\mathrm{Re}\sum_{j,k}[E^v Z_{j,k}Z^\dagger_{j+1,k} + E^h Z_{j,k}Z^\dagger_{j,k+1}], \tag{A1}$$

where E^v and E^h are complex coupling strengths along vertical and horizontal directions of the 2D square lattice, respectively, and Z takes values from $\{1, \omega, \omega^2\}$. (j, k) label site coordinates on the 2D lattice.

The transfer matrix (with periodic boundary conditions) can be written as

$$\mathbb{T} = \sum_{j=0}^{2}(\sigma^\dagger_M)^j l_j \left[\prod_{k=-M}^{M-1}(L_k L_{k+\frac{1}{2}})\right] L_M(\sigma_M)^j, \tag{A2}$$

where the sites are indexed from $[-M, M]$.

$$L_k(u) = \sum_{n=0}^{2}\bar{l}_n(u)\tau_k^n,$$

$$L_{k+\frac{1}{2}}(u) = \sum_{n=0}^{2} l_n(u)(\sigma_k\sigma^\dagger_{k+1})^n.$$

The weights in the transfer matrix, $\bar{l}_1, l_1, \bar{l}_2, l_2$ parametrize E^v, E^{v*}, E^h, E^{h*} of the statistical mechanics model and $l_0 = \bar{l}_0 = 1$.

For a certain range of parameter values, the $\mathbb{Z}_3$ chiral clock model becomes Bethe ansatz integrable. This implies choice of functions $l, \bar{l}$ such that the transfer matrices satisfy Lax pair conditions $[\mathbb{T}(u), \mathbb{T}(u')] = 0$ and $[\mathbb{T}(u), H] = 0$ where H is a quantum Hamiltonian.

Reference [66] considered functions of the form $l_{1,2} = \alpha_{1,2}u + O(u^2)$ and $\bar{l}_{1,2} = \bar{\alpha}_{1,2}u + O(u^2)$ in which case H matches the quantum chiral clock Hamiltonian Eq. (1). The Lax pair conditions can be shown to imply (see Refs. [66,85] for details)

$$\alpha_m \sum_{k=0}^{2}\frac{\bar{S}_{m+k}}{\bar{S}_k}\omega^{-nk} = \bar{\alpha}_n \sum_{k=0}^{2}\frac{S_{n+k}}{S_k}\omega^{-mk} \tag{A3}$$

for $m, n \in \{1, 2\}$ where

$$\bar{S}_m = \sum_{k=0}^{2}\omega^{mk}\bar{l}_k, \quad S_m = \sum_{k=0}^{2}\omega^{mk}l_k, \tag{A4}$$

which can be obtained from the star-triangle relation. These have solutions provided

$$\frac{\alpha_1^3 + \alpha_2^3}{\alpha_1\alpha_2} = \frac{\bar{\alpha}_1^3 + \bar{\alpha}_2^3}{\bar{\alpha}_1\bar{\alpha}_2} \tag{A5}$$

These are equivalent to the integrability condition Eq. (4) using the definitions in Eq. (3) for the chiral clock model. In the rest of the calculations we restrict to the case where $\bar{\alpha}_1 = \bar{\alpha}_2 = \bar{\alpha}$ which corresponds to the case where $\phi = 0$ as was assumed throughout this work.

Logarithm of the transfer matrix is the generator of an infinite set of local conserved charges, i.e.,

$$Q^{(k)} = \lim_{u\to 0}\frac{\mathrm{d}^k}{\mathrm{d}u^k}\ln\mathbb{T}(u) \tag{A6}$$

where $Q^{(k)}$ is the k^{th} conserved charge. In the rest of this section, we calculate $Q^{(1)}, Q^{(2)}, Q^{(3)}$.

At lowest order we get $Q^{(1)}$ to be the quantum Hamiltonian H in Eq. (1). To obtain the higher order terms, we extend the expansion for the functions $l, \bar{l}$ as follows:

$$\begin{aligned} l_n(u) &= \alpha_n u + \beta_n u^2 + \gamma_n u^3 + O(u^4) \\ \bar{l}_n(u) &= \bar{\alpha}_n u + \bar{\beta}_n u^2 + \bar{\gamma}_n u^3 + O(u^4) \end{aligned} \tag{A7}$$

for $n = 1, 2$. Note that β, γ are not complex conjugates of $\bar{\beta}, \bar{\gamma}$. We solve for these additional parameters by inserting Eq. (A7) in Eq. (A3) and equating coefficients of powers of u on both sides.

Equating coefficients of the lowest order in u in Eq. (A3), we get the following solution parametrized by one free parameter:

$$\begin{aligned} \bar{\beta}_1 &= \omega\left(\frac{\bar{\alpha}}{\alpha_2}\alpha_1^2 - \bar{\alpha}^2\right) + \left(\frac{\bar{\alpha}}{\alpha_2}\right)\beta_2, \\ \bar{\beta}_2 &= \omega^2\left(\frac{\bar{\alpha}}{\alpha_2}\alpha_1^2 - \bar{\alpha}^2\right) + \left(\frac{\bar{\alpha}}{\alpha_2}\right)\beta_2, \\ 2(\alpha_1\beta_2 - \alpha_2\beta_1) &= \alpha_1^3 - \alpha_2^3. \end{aligned} \tag{A8}$$

We can plug in solutions of Eq. (A8) in the Eqs. (A7), subsequently expand Eq. (A2) and use Eq. (A6) to get the the conserved charge $Q^{(2)}$ explicitly (this does not depend on the undetermined parameters γs). Demanding Hermiticity and orthogonality of the conserved charge with Hamiltonian at infinite temperature fixes the free parameter in Eq. (A8),

and we obtain

$$Q^{(2)} = \sum_k \Big[I_k + \imath\Big(\frac{1}{2}+\omega\Big)\Big(\frac{\alpha_1^2\bar{\alpha}}{\alpha_2} - \bar{\alpha}^2\Big)\tau_k + \imath\Big(\frac{1}{2}+\omega^2\Big)\Big(\frac{\alpha_1^2\bar{\alpha}}{\alpha_2} - \bar{\alpha}^2\Big)\tau_k^\dagger\Big]. \quad \text{(A9)}$$

Similarly we can constrain γ by comparing the subsequent order in u in Eq. (A3) resulting in the following conditions involving γ and $\bar{\gamma}$:

$$\begin{aligned}
(\omega-1)(\bar{\alpha}\gamma_2 - \alpha_2\bar{\gamma}_2) &= 2(2+\omega)\alpha_2\bar{\alpha}\bar{\beta}_1 + (\omega-4)\alpha_2\bar{\alpha}^3 \\
&\quad - \alpha_1\bar{\alpha}\big(\alpha_2^2(\omega-4) + 2\beta_1(2+\omega)\big), \\
(\omega+2)(\bar{\alpha}\gamma_2 - \alpha_2\bar{\gamma}_1) &= 2(\omega-1)\alpha_2\bar{\alpha}\bar{\beta}_2 + (\omega+5)\alpha_2\bar{\alpha}^3 \\
&\quad - \alpha_1\bar{\alpha}\big(\alpha_2^2(\omega+5) + 2\beta_1(\omega-1)\big), \\
3(\alpha_2\gamma_1 - \alpha_1\gamma_2) &= 2\alpha_2^2\beta_2(-3\omega) - 3(1+2\omega)\alpha_1\alpha_2 \\
&\quad \times (\bar{\alpha}^2 - 2\bar{\beta}_1) - \alpha_1^2(2\beta_1(-3\omega^2) \\
&\quad - 3\alpha_2^2(1+2\omega)). \quad \text{(A10)}
\end{aligned}$$

These have a one parameter set of solutions (for γs; the other parameters were determined in the previous step) which we fix by demanding Hermiticity of $Q^{(3)}$ [its explicit form does not depend on higher order terms omitted in Eq. (A7)] which has the form:

$$\begin{aligned}
Q^{(3)} = \sum_k [& A\sigma_k(\tau_k^\dagger + \tau_{k+1}^\dagger)\sigma_{k+1}^\dagger + B\sigma_k(\tau_k + \tau_{k+1})\sigma_{k+1}^\dagger \\
& - C(\tau_k\sigma_k\tau_{k+1} + \tau_k^\dagger\sigma_k\tau_{k+1}^\dagger)\sigma_{k+1}^\dagger \\
& + C\sigma_k(\tau_k^\dagger\tau_{k+1} + \tau_k\tau_{k+1}^\dagger)\sigma_{k+1}^\dagger \\
& + D\sigma_k(\tau_{k+1} + \tau_{k+1}^\dagger)\sigma_{k+2}^\dagger \\
& + E\sigma_k(\sigma_{k+1}\tau_{k+1} + \tau_{k+1}^\dagger\sigma_{k+1})\sigma_{k+2} \\
& + F\tau_k + G\sigma_k\sigma_{k+1}^\dagger + \text{ h.c. }], \quad \text{(A11)}
\end{aligned}$$

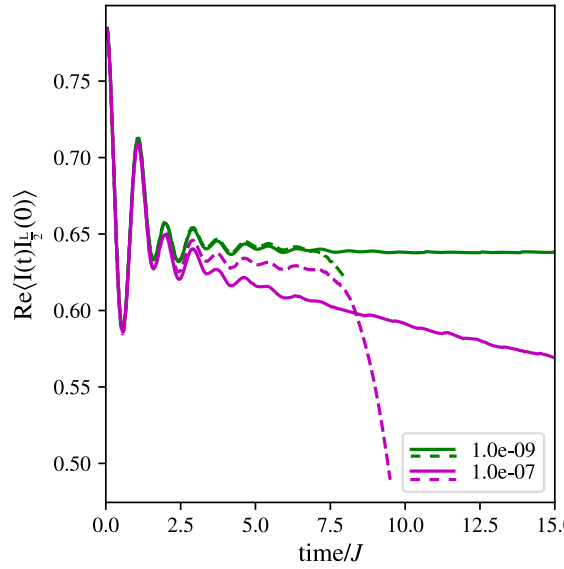

FIG. 11. Similar to Fig. 10 but shows the effect of ancilla disentangler. Solid line is with tDMRG with disentangler unitary and dotted line is without application of ancilla disentangler. Maximum bond dimension is 900 in all cases. $J = 1$, $f = \frac{2}{5}$, $\theta = \cos^{-1}(\frac{2}{5})$, $T = 2$.

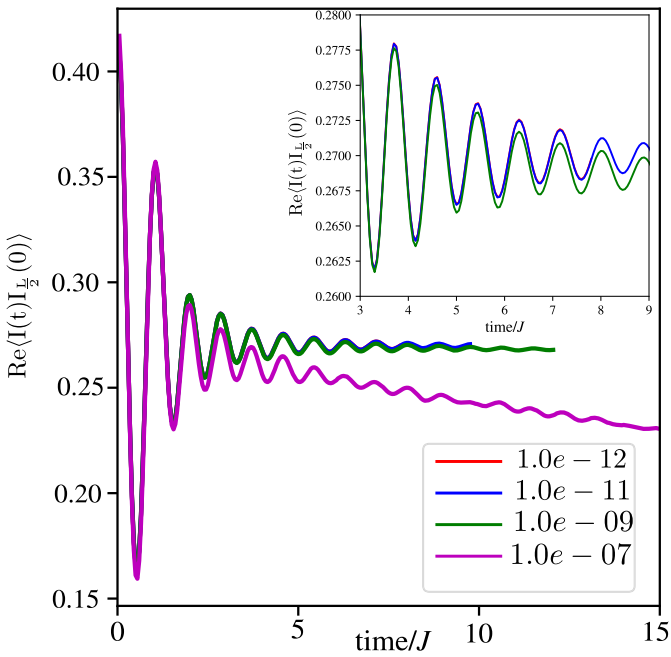

FIG. 10. Convergence of $\mathrm{Re}\langle I(t)I_{L/2}(0)\rangle$ with decreasing truncation cutoff. $J = 1$, $f = \frac{2}{5}$, $\theta = \cos^{-1}(\frac{2}{5})$, $T = 1$. Maximum bond dimension is 900 in all cases. (Inset) Magnified version of the $\mathrm{Re}\langle I(t)I_{L/2}(0)\rangle$ data. Notice the blue and red curves overlap.

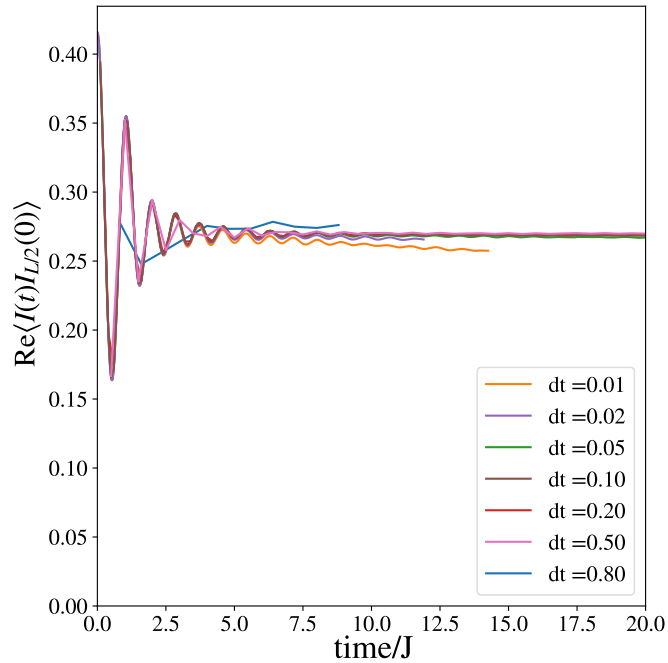

FIG. 12. Convergence of $\mathrm{Re}\langle I(t)I_{L/2}(0)\rangle$ with increasing tDMRG time-step. $J = 1$, $f = \frac{2}{5}$, $\theta = \cos^{-1}(\frac{2}{5})$, $T = 1$. Maximum bond dimension is 900 and cutoff for truncation is 10^{-9} in all cases. Ancilla disentangler is applied during real-time evolution.

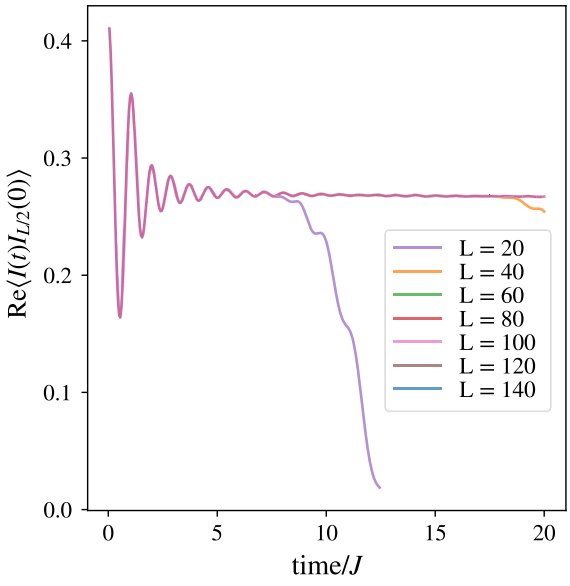

FIG. 13. Convergence of $\mathrm{Re}\langle I(t)I_{L/2}(0)\rangle$ with increasing system size (considering only physical sites). $J = 1$, $f = \frac{2}{5}$, $\theta = \cos^{-1}(\frac{2}{5})$, $T = 1$. Maximum bond dimension is 900 and cutoff for truncation is 10^{-9} in all cases. Ancilla disentangler is applied during real-time evolution.

where

$$A = \frac{\omega^2}{2}\bar{\alpha}\alpha_2^2 - \omega^2\bar{\alpha}^2\alpha_1,$$
$$B = \frac{\omega}{2}\bar{\alpha}\alpha_2^2 - \omega\bar{\alpha}^2\alpha_1,$$
$$C = \bar{\alpha}^2\alpha_1,$$
$$D = -\bar{\alpha}\alpha_1^2,$$
$$E = \omega\bar{\alpha}\alpha_1\alpha_2,$$
$$F = 3\bar{\alpha}\alpha_1\alpha_2,$$
$$G = \frac{3}{2}\bar{\alpha}\alpha_2^2 + \bar{\alpha}^2\alpha_1 + \tfrac{1}{2}\alpha_1^2\alpha_2.$$

Under the operator norm $\langle , \rangle_\rho$ defined in the main text, we find that $Q^{(1)}$ and $Q^{(3)}$ lie in the space perpendicular to $Q^{(2)}$ for all temperatures that we studied in this work. Saturation of the Mazur bound for the current indicates that the current has no component in the space perpendicular to $Q^{(2)}$ which is consistent with explicit numerical calculation of the overlaps of current with $Q^{(1)}$ and $Q^{(3)}$ at finite temperatures.

APPENDIX B: CONVERGENCE OF REAL-TIME DATA FROM tDMRG

Truncation cutoff (ϵ) affects the computational cost and accuracy of tDMRG calculation. We verified the convergence of our current-current correlator by comparing results at different ϵ. For $T = 1$, we observe in Fig. 10 that the truncation cutoff 10^{-9} is sufficient. At larger cutoff (e.g., 10^{-7}), the $\mathrm{Re}\langle \mathrm{I(t)I}_{\frac{\mathrm{L}}{2}}\rangle$ decays fast from around time 5 indicating reliability of the result only up to small time scales. On the other hand, for $\epsilon \leqslant 10^{-9}$ the asymptotic behavior shows very small difference at long time scale indicating convergence of result.

In Fig. 11, we observe that for the same truncation cutoff and bond dimensions, ancilla disentangler produces reliable results for significantly longer time scales.

Data obtained from tDMRG is generally sensitive to time step for evolution (dt) and system size (L). In Fig. 12, it can be observed that time step $\geqslant 0.05$ gives reliable result up to the time scale we observed. The reason for deviation at very short time step (e.g., 0.01, 0.02) can be attributed to accumulation of error incurred from repeated SVD based truncation during

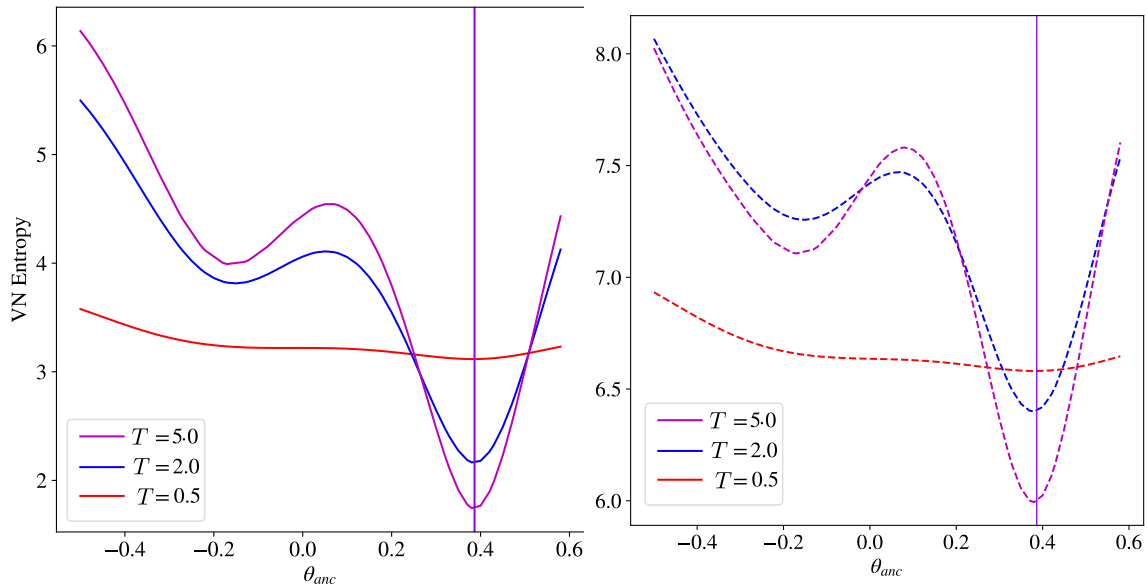

FIG. 14. Optimal value for θ_{anc} decided from the bipartite Von-Neumann entropy on bonds near the quench site. The violet vertical line corresponds to $\theta_{\mathrm{anc}} = \theta$. The solid lines correspond to entanglement growth in thermal state and the dotted lines correspond to entanglement growth in thermal state evolved after quench. The entanglement is measured after time 2.5. Calculations are done at integrable point corresponding to $f = 2/5$ on a system of 30 physical sites.

gate applications (Number of gate applications increase with decreasing time-step for same final time). Also, the correlator estimate deviates for time-step which are too large (e.g dt $\geqslant$ 0.8) due to trotter error.

In Fig. 13, we present the tDMRG data for correlator across different system sizes. System of 60 sites considered in this work is sufficient for reliable estimation of asymptotic value of the correlator. The current-current correlation is non-zero only inside a light cone. Until the light cone hits the boundary, current-current correlator behaves similarly for different system sizes. In smaller systems, the light cone reaches the boundary earlier resulting in a deviation at a shorter time.

APPENDIX C: CHOICE OF FINITE TEMPERATURE DISENTANGLER UNITARY

As noted in the main text, invariance of the reduced density matrix under unitary transformations of the 3^L dimensional ancilla Hilbert space allow us to choose an optimal disentangler unitary transformation of the ancilla that minimize entanglement growth. A search within the 3^{2L} dimensional parameter space of the unitary group $U(3^L)$ is computationally impossible, so we consider a one parameter set of anicilla unitaries of the form $e^{iH_{\rm anc}(\theta_{\rm anc})}$ where $H_{\rm anc}(\theta_{\rm anc})$ has the same form as the clock model Hamiltonian but with a parameter $\theta_{\rm anc}$ replacing θ of the physical Hamiltonian.

We observe that for $\theta_{\rm anc} = \theta$ (Fig. 14), the entanglement growth (as measured by the bipartite Von Neumann entropy) on the bonds near the quench site is minimum at any temperature. The disentangler is most effective at high temperature. Similar conclusion holds for non-integrable points too.

APPENDIX D: CONSISTENCY CHECK OF CONDUCTIVITY DATA

As discussed in Sec. III C, we can evaluate the thermal conductivity using two equivalent expressions [i.e., Eq. (9) and Eq. (15)]. They should result in the same value of $\sigma_{\rm reg}(\Omega)$ if we had the data for correlator till infinite time. However, tDMRG calculation can provide reliable data only up to a finite time scale. Consequently, we incur a "finite-time error" in the discrete Fourier transform required for thermal conductivity calculation Eq. (15). We can estimate this error from the difference in the values obtained from Eq. (9) and Eq. (15). In Figure 15, we provide the data for 3 different temperature at a single point ($f = 2/5$) on integrable line. It can be readily observed that the estimates from Eq. (9) (solid line) and Eq. (15) (dotted line) match quite well for most finite frequency region with significant difference between them only at low frequency. This is expected as low-frequency regime gets most affected by long time data. The estimated error in $\kappa_{\rm reg}(\Omega \to 0)$ is typically an order of magnitude smaller than Drude weight.

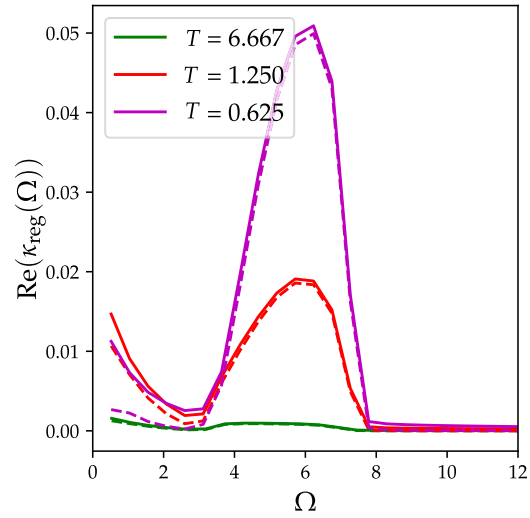

FIG. 15. Re $\kappa_{\rm reg}$ obtained from Eq. (9) is shown in solid line and the same from Eq. (15) is shown in dotted line. Notice both curves overlap for large Ω while deviation can be observed for small Ω.

[1] B. Bertini, F. Heidrich-Meisner, C. Karrasch, T. Prosen, R. Steinigeweg, and M. Žnidarič, Finite-temperature transport in one-dimensional quantum lattice models, Rev. Mod. Phys. **93**, 025003 (2021).

[2] T. Prosen and M. Žnidarič, Matrix product simulations of nonequilibrium steady states of quantum spin chains, J. Stat. Mech.: Theory Exp. (2009) P02035.

[3] I. de Vega and M.-C. Bañuls, Thermofield-based chain-mapping approach for open quantum systems, Phys. Rev. A **92**, 052116 (2015).

[4] C. Karrasch, J. H. Bardarson, and J. E. Moore, Reducing the numerical effort of finite-temperature density matrix renormalization group calculations, New J. Phys. **15**, 083031 (2013).

[5] S. Paeckel, T. Köhler, A. Swoboda, S. R. Manmana, U. Schollwöck, and C. Hubig, Time-evolution methods for matrix-product states, Ann. Phys. **411**, 167998 (2019).

[6] A. Vasiliev, O. Volkova, E. Zvereva, and M. Markina, Milestones of low-d quantum magnetism, npj Quantum Mater. **3**, 18 (2018).

[7] A. A. Belik, M. Azuma, and M. Takano, Characterization of quasi-one-dimensional s=1/2 heisenberg antiferromagnets $Sr_2Cu(PO_4)_2$ and $Ba_2Cu(PO_4)_2$ with magnetic susceptibility, specific heat, and thermal analysis, J. Solid State Chem. **177**, 883 (2004).

[8] T. Kinoshita, T. Wenger, and D. S. Weiss, A quantum Newton's cradle, Nature (London) **440**, 900 (2006).

[9] I. Bloch, J. Dalibard, and S. Nascimbene, Quantum simulations with ultracold quantum gases, Nat. Phys. **8**, 267 (2012).

[10] W. Hofstetter and T. Qin, Quantum simulation of strongly correlated condensed matter systems, J. Phys. B **51**, 082001 (2018).

[11] H. Bernien, S. Schwartz, A. Keesling, H. Levine, A. Omran, H. Pichler, S. Choi, A. S Zibrov, M. Endres, M. Greiner *et al.*, Probing many-body dynamics on a 51-atom quantum simulator, Nature (London) **551**, 579 (2017).

[12] P. Mazur, Non-ergodicity of phase functions in certain systems, Physica **43**, 533 (1969).

[13] M. Suzuki, Ergodicity, constants of motion, and bounds for susceptibilities, Physica **51**, 277 (1971).

[14] X. Zotos, F. Naef, and P. Prelovsek, Transport and conservation laws, Phys. Rev. B **55**, 11029 (1997).
[15] M. Brenes, E. Mascarenhas, M. Rigol, and J. Goold, High-temperature coherent transport in the XXZ chain in the presence of an impurity, Phys. Rev. B **98**, 235128 (2018).
[16] M. Brenes, T. LeBlond, J. Goold, and M. Rigol, Eigenstate Thermalization in a Locally Perturbed Integrable System, Phys. Rev. Lett. **125**, 070605 (2020).
[17] J. De Nardis, S. Gopalakrishnan, R. Vasseur, and B. Ware, Subdiffusive hydrodynamics of nearly integrable anisotropic spin chains, Proc. Natl. Acad. Sci. **119**, e2202823119 (2022).
[18] C. Karrasch, T. Prosen, and F. Heidrich-Meisner, Proposal for measuring the finite-temperature drude weight of integrable systems, Phys. Rev. B **95**, 060406(R) (2017).
[19] P. Prelovšek, M. Mierzejewski, and J. Herbrych, Coexistence of diffusive and ballistic transport in integrable quantum lattice models, Phys. Rev. B **104**, 115163 (2021).
[20] C. Karrasch, J. H. Bardarson, and J. E. Moore, Finite-Temperature Dynamical Density Matrix Renormalization Group And The Drude Weight Of Spin-1/2 Chains, Phys. Rev. Lett. **108**, 227206 (2012).
[21] C. Karrasch, D. M. Kennes, and F. Heidrich-Meisner, Spin and thermal conductivity of quantum spin chains and ladders, Phys. Rev. B **91**, 115130 (2015).
[22] S. Langer, M. Heyl, I. P. McCulloch, and F. Heidrich-Meisner, Real-time energy dynamics in spin-$\frac{1}{2}$ heisenberg chains, Phys. Rev. B **84**, 205115 (2011).
[23] M. Ljubotina, M. Žnidarič, and T. Prosen, Spin diffusion from an inhomogeneous quench in an integrable system, Nat. Commun. **8**, 16117 (2017).
[24] X. Zotos, Finite Temperature Drude Weight of the One-Dimensional Spin-1/2 Heisenberg Model, Phys. Rev. Lett. **82**, 1764 (1999).
[25] A. Urichuk, Y. Oez, A. Klümper, and J. Sirker, The spin drude weight of the XXZ chain and generalized hydrodynamics, SciPost Physics **6**, 005 (2019).
[26] W. Kohn, Theory of the insulating state, Phys. Rev. **133**, A171 (1964).
[27] H. Castella, X. Zotos, and P. Prelovšek, Integrability and Ideal Conductance at Finite Temperatures, Phys. Rev. Lett. **74**, 972 (1995).
[28] B. N. Narozhny, A. J. Millis, and N. Andrei, Transport in the XXZ model, Phys. Rev. B **58**, R2921 (1998).
[29] N. M. R. Peres, P. D. Sacramento, D. K. Campbell, and J. M. P. Carmelo, Curvature of levels and charge stiffness of one-dimensional spinless fermions, Phys. Rev. B **59**, 7382 (1999).
[30] J. Herbrych, P. Prelovšek, and X. Zotos, Finite-temperature Drude weight within the anisotropic heisenberg chain, Phys. Rev. B **84**, 155125 (2011).
[31] D. A. Rabson, B. N. Narozhny, and A. J. Millis, Crossover from Poisson to Wigner-Dyson level statistics in spin chains with integrability breaking, Phys. Rev. B **69**, 054403 (2004).
[32] P. Prelovšek, S. El Shawish, X. Zotos, and M. Long, Anomalous scaling of conductivity in integrable fermion systems, Phys. Rev. B **70**, 205129 (2004).
[33] M. P. Grabowski and P. Mathieu, Structure of the conservation laws in quantum integrable spin chains with short range interactions, Ann. Phys. **243**, 299 (1995).
[34] T. Prosen and E. Ilievski, Families of Quasilocal Conservation Laws and Quantum Spin Transport, Phys. Rev. Lett. **111**, 057203 (2013).
[35] J. Sirker, R. G. Pereira, and I. Affleck, Conservation laws, integrability, and transport in one-dimensional quantum systems, Phys. Rev. B **83**, 035115 (2011).
[36] K. Sakai and A. Klümper, Non-dissipative thermal transport in the massive regimes of the xxz chain, J. Phys. A: Math. Gen. **36**, 11617 (2003).
[37] F. Heidrich-Meisner, A. Honecker, and W. Brenig, Thermal transport of the XXZ chain in a magnetic field, Phys. Rev. B **71**, 184415 (2005).
[38] A. Klümper and K. Sakai, The thermal conductivity of the spin-1/2 XXZ chain at arbitrary temperature, J. Phys. A: Math. Gen. **35**, 2173 (2002).
[39] S. Ajisaka, F. Barra, C. Mejía-Monasterio, and T. Prosen, Nonequlibrium particle and energy currents in quantum chains connected to mesoscopic Fermi reservoirs, Phys. Rev. B **86**, 125111 (2012).
[40] M. Žnidarič, Spin Transport in a One-Dimensional Anisotropic Heisenberg Model, Phys. Rev. Lett. **106**, 220601 (2011).
[41] J. J. Mendoza-Arenas, S. Al-Assam, S. R. Clark, and D. Jaksch, Heat transport in the XXZ spin chain: From ballistic to diffusive regimes and dephasing enhancement, J. Stat. Mech.: Theory Exp. (2013) P07007.
[42] J. J. Mendoza-Arenas, M. Žnidarič, V. K. Varma, J. Goold, S. R. Clark, and A. Scardicchio, Asymmetry in energy versus spin transport in certain interacting disordered systems, Phys. Rev. B **99**, 094435 (2019).
[43] N. Nishad and G. J. Sreejith, Energy transport in chiral clock model, New J. Phys. **24**, 013035 (2022).
[44] L. Mazza, J. Viti, M. Carrega, D. Rossini, and A. De Luca, Energy transport in an integrable parafermionic chain via generalized hydrodynamics, Phys. Rev. B **98**, 075421 (2018).
[45] C. Karrasch, R. Ilan, and J. E. Moore, Nonequilibrium thermal transport and its relation to linear response, Phys. Rev. B **88**, 195129 (2013).
[46] Y. Nozawa and H. Tsunetsugu, Generalized hydrodynamic approach to charge and energy currents in the one-dimensional Hubbard model, Phys. Rev. B **101**, 035121 (2020).
[47] M. Kormos, Inhomogeneous quenches in the transverse field ising chain: Scaling and front dynamics, SciPost Physics **3**, 020 (2017).
[48] X. Zotos, A TBA approach to thermal transport in the XXZ Heisenberg model, J. Stat. Mech.: Theory Exp. (2017) 103101.
[49] B. Bertini and M. Fagotti, Determination of the Nonequilibrium Steady State Emerging from a Defect, Phys. Rev. Lett. **117**, 130402 (2016).
[50] B. Doyon and H. Spohn, Drude weight for the Lieb-Liniger Bose gas, SciPost Phys. **3**, 039 (2017).
[51] S. Langer, F. Heidrich-Meisner, J. Gemmer, I. P. McCulloch, and U. Schollwöck, Real-time study of diffusive and ballistic transport in spin-$\frac{1}{2}$ chains using the adaptive time-dependent density matrix renormalization group method, Phys. Rev. B **79**, 214409 (2009).
[52] C. Karrasch, J. E. Moore, and F. Heidrich-Meisner, Real-time and real-space spin and energy dynamics in one-dimensional spin-$\frac{1}{2}$ systems induced by local quantum quenches at finite temperatures, Phys. Rev. B **89**, 075139 (2014).

[53] S. Jesenko and M. Žnidarič, Finite-temperature magnetization transport of the one-dimensional anisotropic Heisenberg model, Phys. Rev. B **84**, 174438 (2011).
[54] X. Zotos and P. Prelovšek, Evidence for ideal insulating or conducting state in a one-dimensional integrable system, Phys. Rev. B **53**, 983 (1996).
[55] J. S. Ferreira and M. Filippone, Ballistic-to-diffusive transition in spin chains with broken integrability, Phys. Rev. B **102**, 184304 (2020).
[56] F. Heidrich-Meisner, A. Honecker, D. C. Cabra, and W. Brenig, Transport in dimerized and frustrated spin systems, J. Magn. Magn. Mater. **272-276**, 890 (2004).
[57] A. Metavitsiadis, A. Pidatella, and W. Brenig, Thermal transport in a two-dimensional $\mathbb{Z}_2$ spin liquid, Phys. Rev. B **96**, 205121 (2017).
[58] S. Howes, L. P. Kadanoff, and M. Den Nijs, Quantum model for commensurate-incommensurate transitions, Nucl. Phys. B **215**, 169 (1983).
[59] P. Fendley, Parafermionic edge zero modes in zn-invariant spin chains, J. Stat. Mech.: Theory Exp. (2012) P11020.
[60] S. Ostlund, Incommensurate and commensurate phases in asymmetric clock models, Phys. Rev. B **24**, 398 (1981).
[61] D. A. Huse, Simple three-state model with infinitely many phases, Phys. Rev. B **24**, 5180 (1981).
[62] Ye. Zhuang, H. J. Changlani, N. M. Tubman, and T. L. Hughes, Phase diagram of the Z_3 parafermionic chain with chiral interactions, Phys. Rev. B **92**, 035154 (2015).
[63] N. Nishad, M. Santhosh, and G. J. Sreejith, Postquench entropy growth in a chiral clock model, Phys. Rev. B **103**, 195141 (2021).
[64] A. S. Jermyn, R. S. K. Mong, J. Alicea, and P. Fendley, Stability of zero modes in parafermion chains, Phys. Rev. B **90**, 165106 (2014).
[65] P. Fendley, K. Sengupta, and S. Sachdev, Competing density-wave orders in a one-dimensional hard-boson model, Phys. Rev. B **69**, 075106 (2004).
[66] H. Au-Yang, B. M. McCoy, J. H. H. Perk, S. Tang, and Mu. lin Yan, Commuting transfer matrices in the chiral potts models: Solutions of star-triangle equations with genus >1, Phys. Lett. A **123**, 219 (1987).
[67] M. W. Long, P. Prelovšek, S. El Shawish, J. Karadamoglou, and X. Zotos, Finite-temperature dynamical correlations using the microcanonical ensemble and the Lanczos algorithm, Phys. Rev. B **68**, 235106 (2003).
[68] R. Steinigeweg, J. Gemmer, and W. Brenig, Spin-Current Autocorrelations from Single Pure-State Propagation, Phys. Rev. Lett. **112**, 120601 (2014).
[69] F. Heidrich-Meisner, A. Honecker, D. C. Cabra, and W. Brenig, Thermal conductivity of anisotropic and frustrated spin-$\frac{1}{2}$ chains, Phys. Rev. B **66**, 140406(R) (2002).
[70] F. Heidrich-Meisner, A. Honecker, D. C. Cabra, and W. Brenig, Zero-frequency transport properties of one-dimensional spin-$\frac{1}{2}$ systems, Phys. Rev. B **68**, 134436 (2003).
[71] U. Schollwöck, The density-matrix renormalization group in the age of matrix product states, Ann. Phys. **326**, 96 (2011).
[72] C. Karrasch, D. M. Kennes, and J. E. Moore, Transport properties of the one-dimensional hubbard model at finite temperature, Phys. Rev. B **90**, 155104 (2014).
[73] G. Ortiz, E. Cobanera, and Z. Nussinov, Dualities and the phase diagram of the p-clock model, Nucl. Phys. B **854**, 780 (2012).
[74] H. U. Everts and H. Roder, Transfer matrix study of the chiral clock model in the hamiltonian limit, J. Phys. A **22**, 2475 (1989).
[75] J. Motruk, E. Berg, A. M. Turner, and F. Pollmann, Topological phases in gapped edges of fractionalized systems, Phys. Rev. B **88**, 085115 (2013).
[76] R. Samajdar, S. Choi, H. Pichler, M. D. Lukin, and S. Sachdev, Numerical study of the chiral $\mathbb{z}_3$ quantum phase transition in one spatial dimension, Phys. Rev. A **98**, 023614 (2018).
[77] G. Albertini, B. M. McCoy, and J. H. H. Perk, Commensurate-incommensurate transition in the ground state of the superintegrable chiral Potts model, Phys. Lett. A **135**, 159 (1989).
[78] B. M. McCoy and S.-s. Roan, Excitation spectrum and phase structure of the chiral Potts model, Phys. Lett. A **150**, 347 (1990).
[79] J. M. Luttinger, Theory of thermal transport coefficients, Phys. Rev. **135**, A1505 (1964).
[80] R. Kubo, Statistical-mechanical theory of irreversible processes. I. General theory and simple applications to magnetic and conduction problems, J. Phys. Soc. Jpn. **12**, 570 (1957).
[81] R. Haag, N. M. Hugenholtz, and M. Winnink, On the equilibrium states in quantum statistical mechanics, Commun. Math. Phys. **5**, 215 (1967).
[82] T. Barthel, Precise evaluation of thermal response functions by optimized density matrix renormalization group schemes, New J. Phys. **15**, 073010 (2013).
[83] B. S. Shastry, Sum rule for thermal conductivity and dynamical thermal transport coefficients in condensed matter, Phys. Rev. B **73**, 085117 (2006).
[84] J. Sirker, Transport in one-dimensional integrable quantum systems, SciPost Phys. Lect. Notes, 17 (2020).
[85] J. H. H. Perk, The early history of the integrable chiral potts model and the odd–even problem, J. Phys. A **49**, 153001 (2016).
[86] A. Kundu, Quantum integrable systems: Construction, solution, algebraic aspect, arXiv:hep-th/9612046 (1996).
[87] A. E. Feiguin and S. R. White, Finite-temperature density matrix renormalization using an enlarged hilbert space, Phys. Rev. B **72**, 220401(R) (2005).
[88] J. Hauschild, E. Leviatan, J. H. Bardarson, E. Altman, M. P. Zaletel, and F. Pollmann, Finding purifications with minimal entanglement, Phys. Rev. B **98**, 235163 (2018).
[89] D. M. Kennes and C. Karrasch, Extending the range of real time density matrix renormalization group simulations, Comput. Phys. Commun. **200**, 37 (2016).
[90] C. Karrasch, J. Hauschild, S. Langer, and F. Heidrich-Meisner, Drude weight of the spin-1/2 XXZ chain: Density matrix renormalization group versus exact diagonalization, Phys. Rev. B **87**, 245128 (2013).
[91] M. Fishman, S. R. White, and E. M. Stoudenmire, The ITensor software library for tensor network calculations, SciPost Phys. Codebases, 4 (2022).
[92] M. Fishman, S. R. White, and E. M. Stoudenmire, Codebase release 0.3 for ITensor, SciPost Phys. Codebases, 4–r0.3 (2022).
[93] T. Barthel, U. Schollwöck, and S. R. White, Spectral functions in one-dimensional quantum systems at finite temperature using

the density matrix renormalization group, Phys. Rev. B **79**, 245101 (2009).

[94] S. Sachdev and K. Damle, Low Temperature Spin Diffusion in the One-Dimensional Quantum $O(3)$ Nonlinear σ Model, Phys. Rev. Lett. **78**, 943 (1997).

[95] K. Damle and S. Sachdev, Spin dynamics and transport in gapped one-dimensional Heisenberg antiferromagnets at nonzero temperatures, Phys. Rev. B **57**, 8307 (1998).

[96] J. Unfried, J. Hauschild, and F. Pollmann, Fast time evolution of matrix product states using the qr decomposition, Phys. Rev. B **107**, 155133 (2023).

[97] C. D. White, M. Zaletel, R. S. K. Mong, and G. Refael, Quantum dynamics of thermalizing systems, Phys. Rev. B **97**, 035127 (2018).

[98] C. von Keyserlingk, F. Pollmann, and T. Rakovszky, Operator backflow and the classical simulation of quantum transport, Phys. Rev. B **105**, 245101 (2022).